

Controlling Chaos Using Edge Computing Hardware

Robert M. Kent,¹ Wendson A.S. Barbosa,¹ and Daniel J. Gauthier^{1,2,*}

¹The Ohio State University, Department of Physics, 191 West Woodruff Ave., Columbus, OH 43210, USA.

²ResCon Technologies, LLC, 1275 Kinnear Rd., Suite 239, Columbus, OH 43212, USA

*Correspondence to: gauthier.51@osu.edu

May 8, 2024

Abstract

Machine learning provides a data-driven approach for creating a digital twin of a system – a digital model used to predict the system behavior. Having an accurate digital twin can drive many applications, such as controlling autonomous systems. Often, the size, weight, and power consumption of the digital twin or related controller must be minimized, ideally realized on embedded computing hardware that can operate without a cloud-computing connection. Here, we show that a nonlinear controller based on next-generation reservoir computing can tackle a difficult control problem: controlling a chaotic system to an arbitrary time-dependent state. The model is accurate, yet it is small enough to be evaluated on a field-programmable gate array typically found in embedded devices. Furthermore, the model only requires 25.0 ± 7.0 nJ per evaluation, well below other algorithms, even without systematic power optimization. Our work represents the first step in deploying efficient machine learning algorithms to the computing “edge.”

Introduction

We are now in the age of artificial intelligence and machine learning (ML), which is leading to disruptive technologies such as natural language processing,¹ system design optimization,² and autonomous vehicles.³ With these impressive advances, there is a growing interest in applying modern ML tools to existing problems to improve performance and give new insights. One area of recent success is developing advanced controllers for complex dynamical systems, which involves controlling a device or collection of interacting systems that vary in time, such as advanced aircraft, robots, electric motors, among others.

A controller automatically adjusts accessible system parameters based on real-time measurement of the system to guide it to a desired state. Traditional and widely deployed control methods assume that the system responds in a linear fashion to a control adjustment, referred to as a linear controller. However, most systems have a nonlinear response, thereby requiring a precise mathematical model of the system or thorough system characterization and adjusting the linear controller on the fly based on this information.

A particular difficult control task is to stabilize a nonlinear system displaying a complex behavior known as chaos, which is characterized by sensitivity to initial conditions and tiny

perturbations. Previous approaches, such as that pioneered by Ott, Grebogi, and Yorke (OGY)⁴ and by Pyragas,⁵ are restricted to stabilizing unstable states embedded in the dynamics and are restricted to making small adjustments to the accessible system parameters and hence control can only be turned on once the system is close to a desired state.

Machine-learning-based controllers offer a new approach that has the advantage of learning the nonlinear properties of the system based only on data, relearning the system dynamics to respond to system degradation over time⁶ or damage events,⁷ and monitoring system health and status.⁸ However, recent ML solutions are often computationally expensive, requiring computational engines such as power-hungry graphical processor units, or developing custom neuromorphic chips using analog-digital designs or advanced materials that operate at low power.⁹⁻¹¹

An alternative approach is to simplify the ML algorithm so that it can be deployed on commercial off-the-shelf microcontrollers or field-programmable gate arrays (FPGAs). These compute devices are small and consume low power, thus making them well-suited for edge-computing and portable devices without requiring a connection to cloud-computing resources. One candidate approach is to use a reservoir computer^{12,13} (RC), a best-in-class ML algorithm for learning dynamical systems. Previous work by Canaday *et al.*¹⁴ used a RC to learn an inverse-based control algorithm, but it failed to achieve accurate control. We believe these shortcomings are due to the learned inverse not being unique or due to control-loop latency that was not learned.

To avoid these problems, we use a feedback linearization algorithm combined with a highly efficient next-generation reservoir computer (NG-RC)¹⁵ that greatly simplifies the controller and reduces the computational resources. Here the NG-RC predicts the future state of the system, which is feedback via the controller to cancel the nonlinear terms of the systems nonlinear dynamical evolution while simultaneously providing linear feedback to stabilize the system to the desired time-dependent state.

We demonstrate that an NG-RC-based controller can stabilize the dynamics of a chaotic electronic circuit¹⁶ to trajectories that are impossible for classic chaos control methods and has lower error than the inverse-control algorithm used by Canaday *et al.*¹⁴ as well as a linear controller. We implement our design using a FPGA on a commercial demonstration board to collect real-time data from the circuit, process the data using a firmware-based NG-RC, and apply the control perturbations. An FPGA has the advantage that it can perform parallel computations well matched to our ML algorithm and it has memory co-located with the processing logic gates, which is known to boost efficiency.^{10,11} Furthermore, the ML algorithm is so simple and efficient that its execution time is much faster than other system processes and its power consumption is a tiny fraction of the overall power budget.

Below, we give an overview of our experimental system, introduce the control algorithm, and provide an overview of reservoir computing. We then present our results on suppressing chaos in the circuit by guiding the system to desired states and give key performance metrics. We close with a comparison to other recent ML-based control approaches and discuss how our controller can be further improved with optimized hardware.

Results

An overview of our prototype chaotic circuit and nonlinear control system is shown in Fig. 1. The chaotic circuit (known as the “plant” in the control literature) consists of passive components including diodes, capacitors, resistors, and inductors, and an active negative resistor realized with an operational amplifier that can source and sink power to the rest of the circuit. The phase space of the system is three-dimensional specified by voltages V_1 and V_2 across two capacitors in the circuit and the current I passing through the inductor (see Methods). To display chaos, the circuit must be nonlinear, which arises from the diodes as evident from their nonlinear current-voltage relation. We adjust the circuit parameters so that it displays autonomous double-scroll chaotic dynamics characterized by a positive Lyapunov exponent, indicating chaotic dynamics.¹⁶ A two-dimensional projection of the phase space trajectory allows us to visualize the corresponding strange attractor and is shown in Fig. 1.

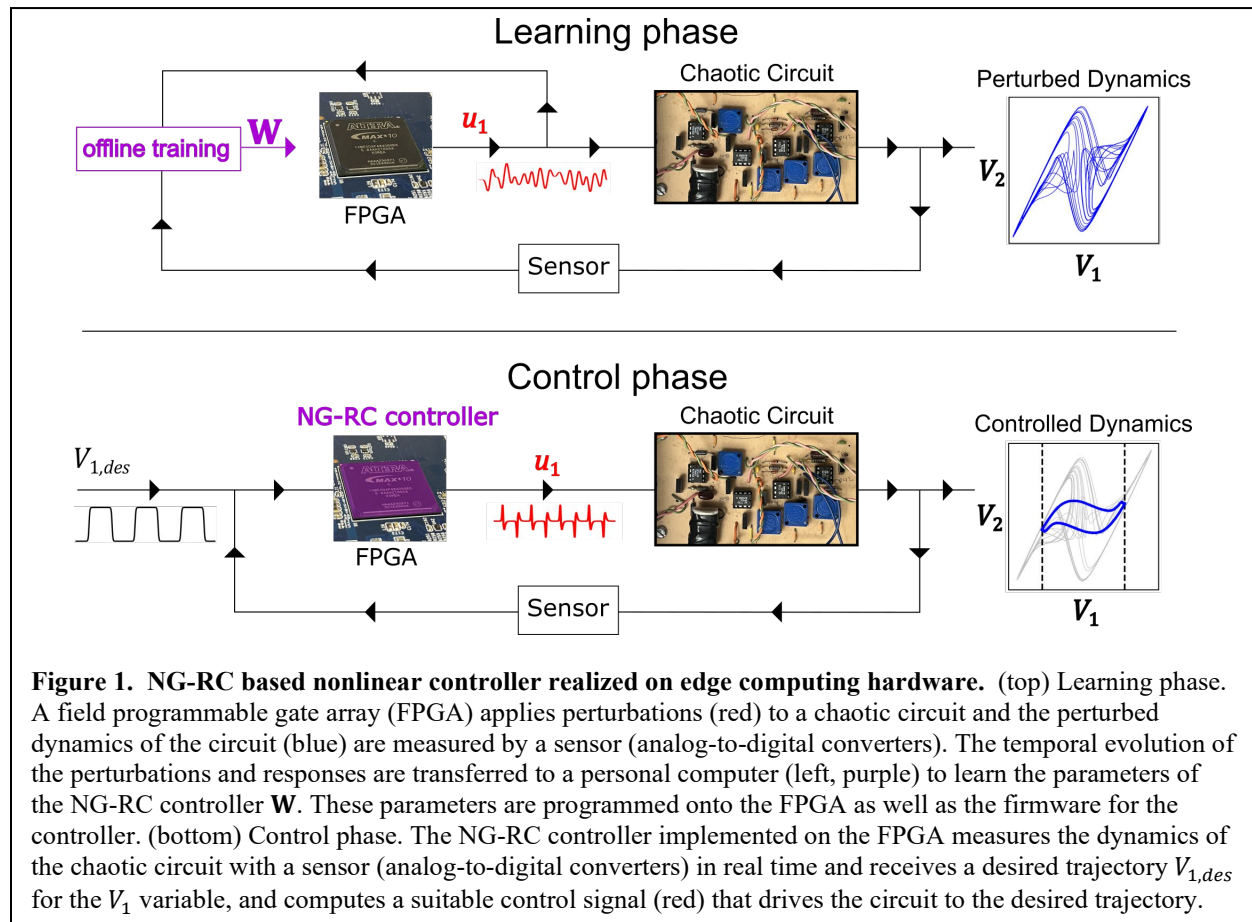


Figure 1. NG-RC based nonlinear controller realized on edge computing hardware. (top) Learning phase. A field programmable gate array (FPGA) applies perturbations (red) to a chaotic circuit and the perturbed dynamics of the circuit (blue) are measured by a sensor (analog-to-digital converters). The temporal evolution of the perturbations and responses are transferred to a personal computer (left, purple) to learn the parameters of the NG-RC controller \mathbf{W} . These parameters are programmed onto the FPGA as well as the firmware for the controller. (bottom) Control phase. The NG-RC controller implemented on the FPGA measures the dynamics of the chaotic circuit with a sensor (analog-to-digital converters) in real time and receives a desired trajectory $V_{1,des}$ for the V_1 variable, and computes a suitable control signal (red) that drives the circuit to the desired trajectory.

To control the system, we measure in real time two accessible variables – voltages V_1 and V_2 – using analog-to-digital converters located on the FPGA (the sensors indicated in Fig. 1). We are limited to measuring two variables because of the available resources on the device. For a similar reason, we are limited to controlling a single variable, which we take as V_1 based on previous control experiments with this circuit.¹⁶ Here, the user provides a desired value $V_{1,des}$ as the control target, which can be time-dependent.

The goal of the controller is to guide the system to the desired state by perturbing its dynamics based on a nonlinear control law. Controlling this system to a wide range of behaviors requires that the controller also be nonlinear; the applied perturbations are a nonlinear function of

the measured state variables. Importantly, a nonlinear controller allows us to go beyond established chaos control methods that are restricted to controlling about sets embedded in the dynamics and only applying control when the system is close to one of these sets,^{4,17,18} as mentioned above.

Coming back to the control implementation, we use two phases: 1) a learning phase where we learn the dynamics of the chaotic circuit and how it responds to random perturbations (Fig. 1, top panel) in an “open” configuration; and 2) a closed-loop configuration (Fig. 1, bottom panel), where the learned model generates perturbations based on the real-time measurements and the user-specified desired state. We store the desired state in local on-chip memory to reduce the system power consumption, but it is straightforward to interface our controller with a higher-level system manager or user interface to allow greater flexibility.

During the training phase, we synthesize a low-pass-filtered random sequence and store it in on-chip memory (see Methods). This sequence is read out of memory and sent off-chip to a digital-to-analog converter, which passes to a custom-built voltage-to-current converter (u_1 in the top panel of Fig. 1, red waveform) and injected into the chaotic circuit at the node corresponding to the capacitor giving rise to voltage V_1 .

The control current perturbs the chaotic dynamics so we can learn how it responds to perturbations at many locations in phase space, which is common in extremum-seeking control,¹⁹ for example. To this end, we simultaneously measure the voltages V_1 and V_2 and store their values in on-chip memory. After a training session, the data is transferred to a laptop computer to determine the NG-RC model as described below. The model is then programmed in the FPGA logic.

Nonlinear control is turned on by “closing the loop.” Here, the real-time measured voltages and the desired state are processed by the NG-RC model, control perturbations calculated, and subsequently injected into the circuit. There is always some latency between measurements and perturbation, which can destabilize the control if it becomes comparable to or larger than the Lyapunov time – the interval over which chaos causes signal decorrelation.²⁰ We optimize the overall system timing to minimize the latency, but the NG-RC model and control law is so simple that the evaluation time is two orders of magnitude shorter than the other latencies present in the controller, which are detailed Supplementary Note 7. Another important aspect of our controller is that we use fixed-point arithmetic, which is matched to the digitized input data and reduces the required compute resources and power consumption.¹⁰

Control Law

We formalize the control problem as follows: the accessible variables of the chaotic circuit $\mathbf{X} \in \mathbb{R}^{d'}$ are the inputs to a nonlinear control law that specifies the control perturbations $\mathbf{u} \in \mathbb{R}^d$ ($d \leq d'$) necessary to guide a subset of the accessible system variables $\mathbf{Y} \in \mathbb{R}^d$ to a desired state $\mathbf{Y}_{des} \in \mathbb{R}^d$. We assume the dynamics of the system evolve in continuous time, but discretely sampled data allows us to describe the dynamics of the uncontrolled system in the absence of noise by the mapping

$$\mathbf{X}_{i+m} = \mathbf{F}'_{i+m}(\mathbf{X}_i, \mathbf{X}_{i-1}, \dots, \mathbf{X}_{i-(k-1)}), \quad (1)$$

where i represents the index of the variables at time t_i , m is the number of timesteps the map projects into the future and $\mathbf{F}'_{i+m} \in \mathbb{R}^{d'}$ is a nonlinear function specifying the flow of the system, which may depend on k past values of the system variables. The dynamics of the

controlled variables are then given by $\mathbf{Y}_{i+m} = \mathbf{F}_{i+m}$, where $\mathbf{F}_{i+m} \in \mathbb{R}^d$ is related to \mathbf{F}'_{i+m} through a projection operator. We assume the control perturbations at time t_i affect the dynamics linearly, while past values may have nonlinear effects on the flow of the system, allowing us to express the dynamics of the controlled system variables as

$$\mathbf{Y}_{i+m} = \mathbf{F}_{i+m}(\mathbf{X}_i, \mathbf{X}_{i-1}, \dots, \mathbf{X}_{i-(k-1)}, \mathbf{u}_{i-1}, \dots, \mathbf{u}_{i-(k-1)}) + \mathbf{W}_u \mathbf{u}_i, \quad (2)$$

where we omit the arguments of \mathbf{F}_{i+m} below for brevity.

To control a dynamical system of the form (2), we use a general nonlinear control algorithm developed for discrete-time systems.²¹ Different from many previous nonlinear controllers,²² we do not require a physics-based model of the plant. Rather, we use a data-driven model learned during the training phase. Robust and stable control of the dynamical system is obtained^{21,23} by taking

$$\mathbf{u}_i = \widehat{\mathbf{W}}_u^{-1} [\mathbf{Y}_{des,i+m} - \widehat{\mathbf{F}}_{i+m} + \mathbf{K} \mathbf{e}_i], \quad (3)$$

where, $\mathbf{Y}_{des,i+m} \in \mathbb{R}^d$ is the desired state of the system m -steps-ahead in the future, $\mathbf{K} \in \mathbb{R}^{d \times d}$ is a closed loop gain matrix, and $\mathbf{e}_i = \mathbf{Y}_i - \mathbf{Y}_{des,i}$ is the tracking error. The “^” over the symbols indicate that these quantities are learned during the training phase using the procedure described in the next subsection. A key assumption is that we can learn \mathbf{F}_{i+m} only using information from the accessible system variables and past perturbations.

The control law (3) executes feedback linearization, where the feedback attempts to cancel the nonlinear function \mathbf{F}_{i+m} in mapping (2), thus reducing to a linear control problem. To see this, assume perfect learning ($\widehat{\mathbf{F}}_{i+m} = \mathbf{F}_{i+m}$, $\widehat{\mathbf{W}}_u = \mathbf{W}_u$), and apply the definition of the tracking error to obtain

$$\mathbf{e}_{i+1} = \mathbf{K} \mathbf{e}_i. \quad (4)$$

This system is globally stable when all eigenvalues of \mathbf{K} are within the unit circle. Adjustments to \mathbf{K} are required to maintain globally stable control in the presence of bounded modeling error and noise.²¹

For comparison, we compare our nonlinear controller to a simple linear proportional feedback controller. We can make a simple adjustment to the control law described above to realize a linear controller. Consider the case when the sampling time Δt is short relative to the timescale of the system’s dynamics, allowing us to approximate the flow $\widehat{\mathbf{F}}_{i+m}$ in the control law (3) with the current state \mathbf{Y}_i to arrive at a linear control law. This is motivated by approximating the flow using Euler integration with a single step $\mathbf{Y}_{i+1} \approx \mathbf{Y}_i + \Delta t \mathbf{f}(t_i, \mathbf{X}_i)$, where $\mathbf{f}(t_i, \mathbf{X}_i)$ is the vector field governing the dynamics, and observing that $\mathbf{Y}_{i+1} \approx \mathbf{Y}_i$ when Δt approaches zero.

Based on the number of accessible system variables and control perturbations in our system, we take $d' = 2$ and $d = 1$ corresponding to $\mathbf{X}_i = [V_{1,i}, V_{2,i}]^T$, $\mathbf{Y}_i = V_{1,i}$, $\mathbf{u}_i = u_{1,i}$, and the feedback control gain K is a scalar. Additionally, we take $m = 1$ (2) in this work for one-step- (two-step-) ahead prediction, as this provides a trade-off between controller stability and accuracy.

Reservoir Computing

Here, we briefly summarize the NG-RC algorithm^{12,13} used to estimate $\widehat{\mathbf{W}}_u^{-1}$ and $\widehat{\mathbf{F}}$ needed for the control law. Like most ML algorithms, an RC maps input signals into a high-dimensional space to increase computational capacity, and then projects the system onto the desired low-dimensional output. Different from other popular ML algorithms, RCs have natural fading memory, making them particularly effective at learning the behavior of dynamical systems.

A RC gains much of its strength by using a linear-in-the-unknown-parameters universal representation²⁴ for $\widehat{\mathbf{F}}$, which vastly simplifies the learning process that uses linear regularized least-squares optimization. The other strength is that the number of trainable parameters in the model is smaller than other popular ML algorithms, thus reducing the size of the training dataset and the compute time for training and deployment. Previous studies have successfully used an RC to control a robotic arm²⁵ and a chaotic circuit,¹⁴ for example, using an inverse-control method.²⁶

The next-generation reservoir computing algorithm has similar characteristics to a traditional RC,²⁷ but has fewer parameters to optimize, requires less training data, and is less computationally expensive.¹⁵ In this framework, the function $\widehat{\mathbf{F}}$ is represented by a linear superposition of nonlinear functions of the accessible system variables \mathbf{X} at the current and past times, as well as perturbations \mathbf{u} at past times, as mentioned previously. The number of time-delayed copies k of these variables form the memory of the NG-RC. Based on previous work on learning the double-scroll attractor,¹⁵ we use $k = 2$ and use odd-order polynomial functions of \mathbf{X} up to cubic order, but we only take linear functions of past perturbations \mathbf{u}_{i-1} for simplicity. The feature vector also contains the perturbations \mathbf{u}_i , which allows us to estimate $\widehat{\mathbf{W}}_u$. We perform system identification^{28,29} to select the most important components of the model. Additional details regarding the NG-RC implementation are given in the Methods.

Control Tasks

We apply our nonlinear control algorithm with three challenging tasks. The first is to control the system to the unstable steady state (USS) located at the origin [$V_1 = 0$, $V_2 = 0$, $I = 0$] of phase space starting from a random point located on the strange attractor. Previous work by Chang *et al.*¹⁶ fail to stabilize the system at the origin using an extended version of the Pyragas approach.³⁰

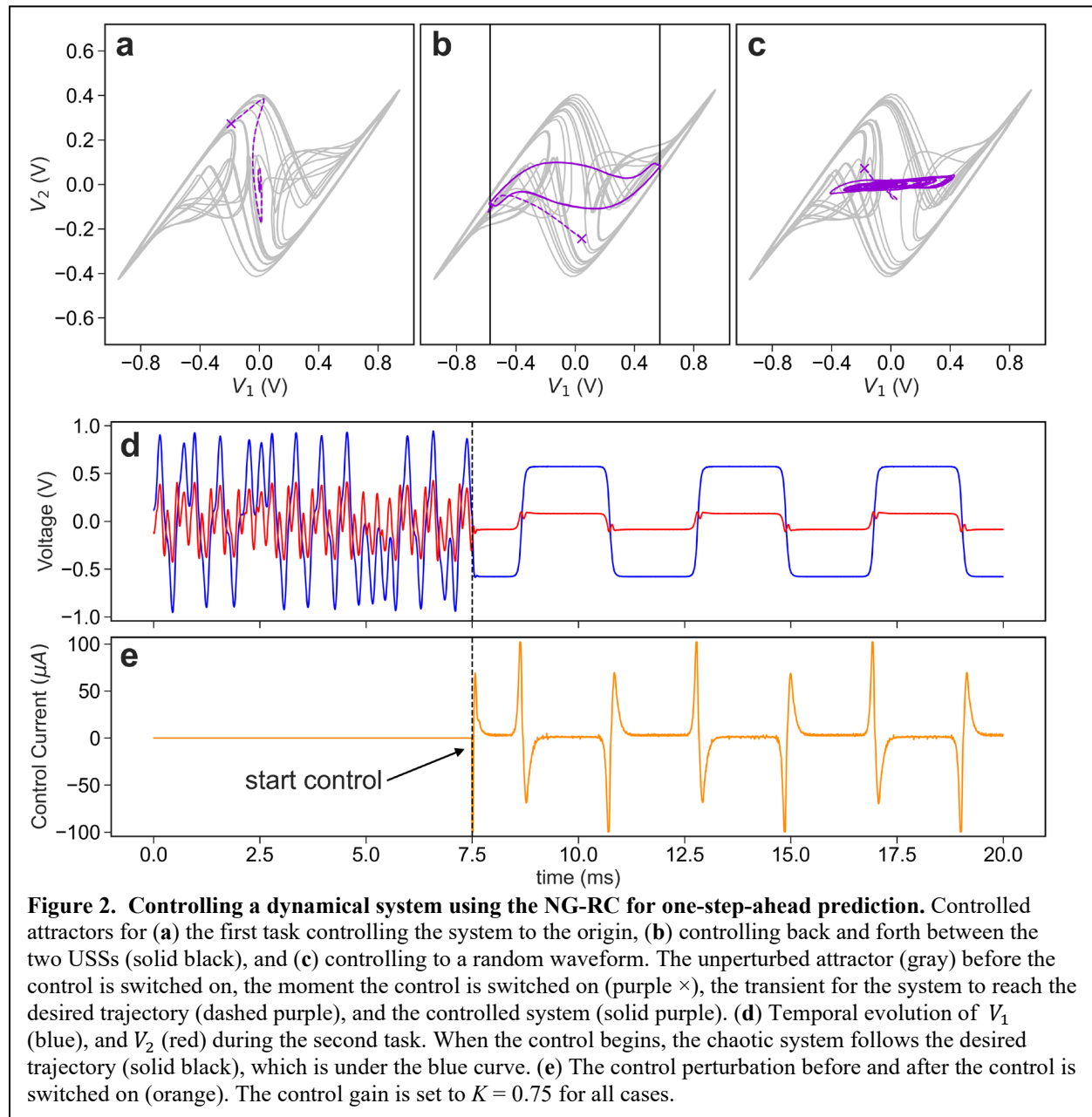
The second task is to control the system about one of the USSs in the middle of one of the “scrolls” and then guide the system to the USS at the other scroll and then back in rapid succession. Rapid switching between these USSs is unattainable using Pyragas-like approaches because the controller must wait for the system to cross into the opposite basin of attraction defined by the line $V_I = 0$,¹⁶ which cannot occur within the requested transition time. Additionally, the system never visits the vicinity of these USSs¹⁶ and hence large perturbations are required to perform the fast transitions, causing the OGY⁴ approach to fail.

Last, we control the system to a random trajectory, which determines if the system can be controlled to an arbitrary time-dependent state. This task is difficult because the controller must cancel the nonlinear dynamics at all points in phase space, requiring an accurate model of the flow. This task is infeasible for Pyragas-like approaches, as they are limited to controlling the system to UPOs and USSs. There are extensions of the OGY method that can steer the system to arbitrary points on the attractor,³¹ but controlling between arbitrary points quickly requires large perturbations, making this approach unsuitable. Furthermore, this approach can require significant memory to store paths to the desired state,³² increasing the power and resource consumption.

Example Trajectories

Example phase-space trajectories of the controlled system for the three different tasks are shown in Fig. 2. For the first, the dynamics of the system are far from the origin when the controller is turned on (indicated by an \times in the phase portrait) and quickly evolves toward the origin and remains stable for the remainder of the control phase. Note that we only control V_1 ; V_2 and I (not shown) are naturally guided to zero through their coupling to V_1 .

For the second task, it is seen that V_1 and V_2 are successfully guided to the corresponding values of the USSs. The trajectory followed by the system as it transitions between the USSs depends on the requested transition rate because changes in V_2 lags changes in V_1 as governed by

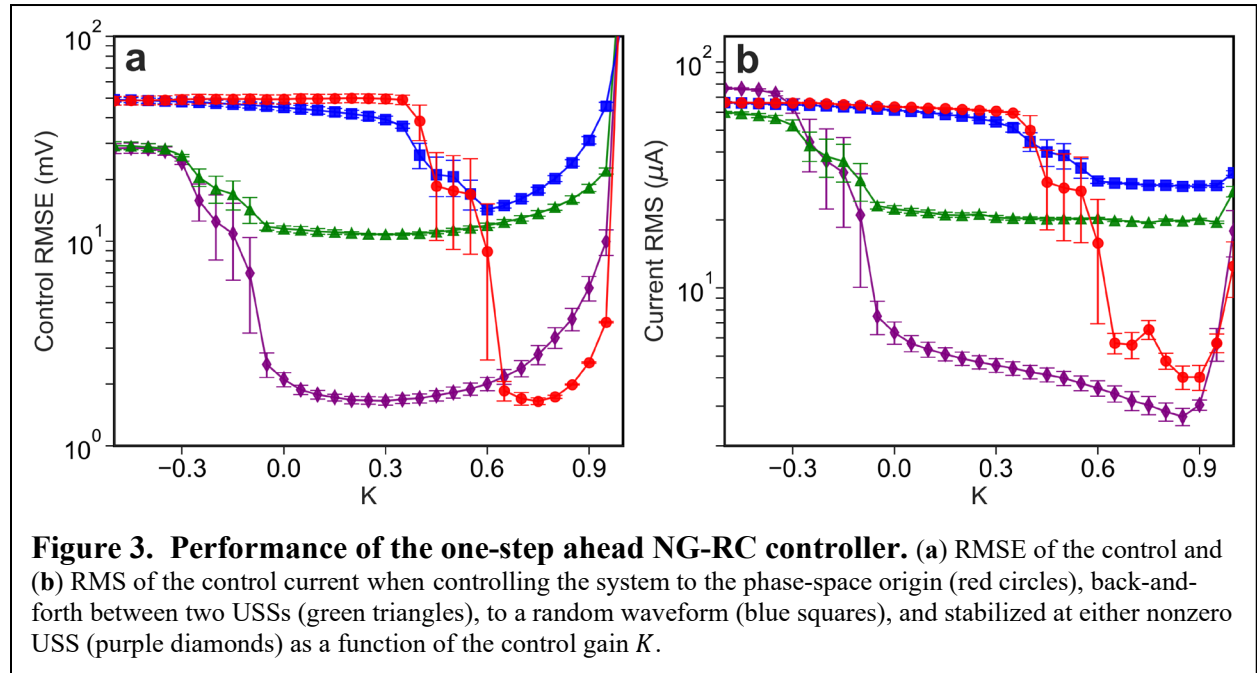


their nonlinear coupling. The temporal evolution of the system is shown in Figs. 2d-e, where we see that V_1 accurately follows the desired trajectory without any visible overshoot.

For the final task, we request that V_1 follows a random trajectory contained within the domain of the strange attractor as shown in Fig. 2c; additional results visualizing the controlled system is given in Supplementary Note 2.

Control Performance

We now characterize the stability of the nonlinear controller as a function of the feedback gain K and compare the control error on the three tasks for the linear and nonlinear controllers. Figure 3 shows the performance of the controller as K varies, where Fig. 3a shows the error between the requested and actual state of the system, while Fig. 3b shows the size of the control perturbations. We see that there is a broad range of feedback gains that give rise to high-quality control, and the control perturbations are small at the USSs, showing the robustness of our approach. The domain of control is somewhat smaller than that expected, which we believe is due to small modeling errors and latency between measuring the state and applying the control perturbation.^{20,33} We find that the NG-RC controller with two-step-ahead prediction has a substantially larger domain of control, which is detailed in Supplementary Note 3.



The minimum error for each task and controller type is given in Table 1. We see that the NG-RC controllers outperforms the linear controller on every task, except when the system is stabilized at the nonzero USSs because the dynamics are approximately linear there.

The advantage of the NG-RC controller is evident for the random waveform task, where we observe a $1.7\times$ reduction in the error compared to the linear controller. This task is especially challenging for the linear controller because the desired state visits a wide range of phase space with different local linear dynamics and the sampling rate is too slow for $\mathbf{Y}_{i+1} \approx \mathbf{Y}_i$ to be a good approximation, making the controller ineffective at cancelling the nonlinear dynamics of the system. Additional performance metrics, such as the error, size of control perturbations, and sensitivity to control-loop latency are given in the Supplementary Note 3.

Table 1 Minimum control error

Controller type	Origin task	Two USS task	Two USS task (no transients)	Random waveform task
Linear	$2.61 \pm 0.11\text{mV}$	$11.98 \pm 0.51\text{mV}$	$1.67 \pm 0.05\text{mV}$	$25.10 \pm 1.90\text{mV}$
one-step ahead	$1.65 \pm 0.06\text{mV}$	$10.79 \pm 0.07\text{mV}$	$1.65 \pm 0.08\text{mV}$	$14.23 \pm 0.24\text{mV}$
two-step ahead	$1.64 \pm 0.02\text{mV}$	$11.23 \pm 0.26\text{mV}$	$1.95 \pm 0.11\text{mV}$	$14.57 \pm 0.44\text{mV}$

The minimum RMSE for each controller type and control task with uncertainty derived from the standard error over five trials.

Control Resources

We now discuss the resources needed for implementing control. First, the FPGA demonstration board has resources well matched to the chaotic system. The characteristic timescale of the chaotic circuit is $24 \mu\text{s}$, which compares favorably with the 1 Msample/s sampling rate of the analog-to-digital and digital-to-analog converters and our control update period of $5 \mu\text{s}$. Unlike previous ML-based controllers, the update period is not limited by the evaluation time of the ML model and control law, which only requires a computation time of 50 ns .

Regarding power consumption, our demonstration board is not designed for low-power operation and there is a substantial power-on penalty when using the board. For the NG-RC-based controllers, we observe a total power consumption of $1384.0 \pm 0.7 \text{ mW}$, where $53.5 \pm 1.4 \text{ mW}$ is consumed by the analog-to-digital and digital-to-analog converters, $5.0 \pm 1.4 \text{ mW}$ is consumed evaluating the NG-RC algorithm, and the remainder is for other on-board devices not used directly by the control algorithm. Considering the control loop rate of 200 kHz , these results indicate that we only expend $25.0 \pm 7.0 \text{ nJ}$ per inference if we consider only the energy consumed by the NG-RC, or $6,920.0 \pm 3.5 \text{ nJ}$ considering the total power. In contrast, the linear controller requires only $7.5 \pm 7.0 \text{ nJ}$ per inference, which is primarily due to the decreased number of multiplications.

Regarding the logic and math resources on the FPGA, the one-step ahead controller uses 1722 logic elements (3% of the available resources), 924 registers (1.8%), and 18 multipliers (13%). The two-step ahead controller requires 16 additional registers to store the desired state two steps in the future, but otherwise uses the same resources. In contrast, the linear controller uses 986 (2%) logic elements, 604 registers (1.2%), and 4 multipliers. All controllers use only 768 memory bits (<1%) for the origin task, which does not require any additional memory to store the desired signal. These resources are small in comparison to other recent ML-based control algorithms evaluated on an FPGA, which we present in Supplementary Note 4. Additionally, we show that the computational complexity of our approach is significantly lower than the RC-based inverse controller by Canaday *et al.*¹⁴ in Supplementary Note 1.

Discussion

We provide a proof-of-concept demonstration of using a state-of-the-art ML algorithm to control a complex dynamical system deployed on a small size and low power embedded computing device. The nonlinear controller uses very few resources when implemented on an

FPGA, it's highly parallelizable resulting in an inference time on the nanosecond timescale, and it is robust to modeling and discretization error, delays, and noise. Even though we do not use a power-efficient device, it consumes less energy per inference than most ML-based controllers.

When compared to a linear controller, our approach achieves a $1.7\times$ smaller error on the most difficult control task, requiring only a small increase in the percentage of available FPGA resources and the power consumption. Furthermore, we achieve better performance than the RC-based inverse control law approach by Canaday *et al.*¹⁴ while using $4\times$ less training data, $6\times$ fewer trainable parameters, $30\times$ fewer multiplications, and 60 fewer evaluations of the hyperbolic tangent function. Additionally, we use 18-bit arithmetic rather than 32-bit arithmetic, which uses fewer resources on the FPGA device. These differences demonstrate that a nonlinear controller based on the NG-RC algorithm achieves higher performance using substantially few compute resources.

There are several directions to improve upon our results. One is to perform the training directly on the FPGA using on-line regularized regression, as mentioned above. Another is to apply the controller to higher-dimensional problems such as spatial-temporal dynamics.³⁴ Regarding the power consumption, it can be likely be reduced to the sub-mW level using a more power-efficient FPGA on a custom circuit board without extraneous components. Because our algorithm only requires a small number of multiplications and additions, the model can be evaluated efficiently on the recent custom artificial-intelligence processors^{10,11} or using a custom application-specific integrated circuit to achieve the lowest power consumption.

Methods

Next generation reservoir computing

We use a next-generation reservoir computer to estimate \mathbf{F} and \mathbf{W}_u . The first step is to construct a *linear feature vector* containing the measured variables \mathbf{X}_i as well as k time-delays as

$$\mathbb{O}_{lin,i} = \mathbf{X}_i \oplus \mathbf{X}_{i-1} \oplus \mathbf{X}_{i-2} \oplus \dots \oplus \mathbf{X}_{i-(k-1)}. \quad (5)$$

where \oplus is the concatenation operation. To suitably approximate the nonlinearities in $\hat{\mathbf{F}}$, nonlinear functions of $\mathbb{O}_{lin,i}$ are required, which are often taken to be polynomials as they can be used to approximate the dynamics of many systems. After the nonlinear feature vector $\mathbb{O}_{nonlin,i}$ is constructed, all features that relate to \mathbf{X}_i can be combined in the feature vector

$$\mathbb{O}_{\mathbf{X},i} = c \oplus \mathbb{O}_{lin,i} \oplus \mathbb{O}_{nonlin,i}, \quad (6)$$

where c is a constant, which is not required in this case because there is no constant in the differential equations that describe the dynamics of V_1 in the chaotic circuit in Eq. 12. The feature vector used to estimate \mathbf{F} is then given by

$$\mathbb{O}_{\mathbf{F},i} = \mathbf{u}_{i-1} \oplus \mathbb{O}_{\mathbf{X},i}, \quad (7)$$

where only a single past perturbation \mathbf{u}_{i-1} is used because we choose $k = 2$. Lastly, we construct the total feature vector

$$\mathbb{O}_{total,i} = \mathbf{u}_i \oplus \mathbb{O}_{\mathbf{F},i}, \quad (8)$$

and learn the weights \mathbf{W} that map $\mathbb{O}_{total,i}$ onto \mathbf{Y}_{i+1} , or

$$\mathbf{Y}_{i+m} \approx \mathbf{W}\mathbb{O}_{total,i} = \widehat{\mathbf{W}}_{\mathbf{F}}\mathbb{O}_{\mathbf{F},i} + \widehat{\mathbf{W}}_u\mathbf{u}_i, \quad (9)$$

where $\widehat{\mathbf{W}}_{\mathbf{F}}$ are the weights that relate to the \mathbf{F} , and $\widehat{\mathbf{W}}_u^{-1}$ can be computed to complete the control law. If learning is perfect, then $\widehat{\mathbf{W}}_{\mathbf{F}}\mathbb{O}_{\mathbf{F},i} = \mathbf{F}_{i+m}$ and $\widehat{\mathbf{W}}_u = \mathbf{W}_u$. The learning process involves computing \mathbf{W} using ridge regression,³⁵ which has the explicit solution

$$\mathbf{W} = \mathbf{Y}_d\mathbb{O}_{total}^T(\mathbb{O}_{total}\mathbb{O}_{total}^T + \alpha\mathbf{I})^{-1}, \quad (10)$$

where \mathbf{Y}_d contains \mathbf{Y}_{i+m} , and \mathbb{O}_{total} contains $\mathbb{O}_{total,i}$, for all times t_i in the training data set, and α is the ridge parameter that can be tuned to prevent overfitting.

The learned weights are then used to perform predictions on a validation data set, and the prediction performance is evaluated using the root mean square error

$$\text{RMSE} = \sqrt{\langle (x_i - \hat{x}_i)^2 \rangle}, \quad (11)$$

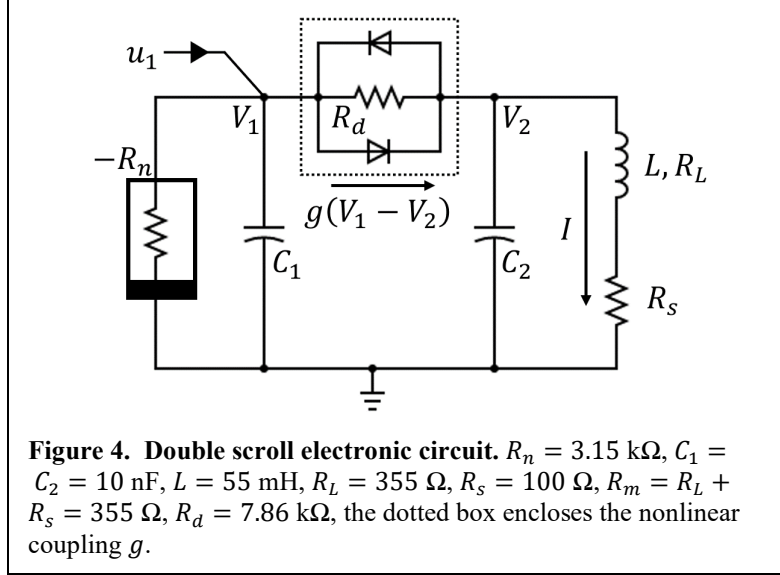
where x_i is the true value and \hat{x}_i is the predicted value. The ridge parameter is tuned so that the prediction RMSE on the validation data is minimized. This metric is also used to characterize the control performance, where x_i is the desired signal, and \hat{x}_i is the state of the controlled system.

Double scroll circuit

The dynamics of the chaotic circuit shown in Fig. 4 are described by the differential equations

$$\begin{aligned} C_1\dot{V}_1 &= V_1/R_n - g(V_1 - V_2) + u_1, \\ C_2\dot{V}_2 &= g(V_1 - V_2), \\ L\dot{I}_1 &= V_2 - R_m \end{aligned} \quad (12)$$

where $g(V) = V/R_d + 2I_r \sinh(\alpha V/V_d)$, $I_r = 5.63$ nA, $\alpha = 11.6$, $V_d = 0.58$ V, and u_1 is the accessible control current. The USSs are [$V_1=0.58$ V, $V_2 = 0.08$ V, $I=0.20$ mA] and [$V_1=-0.58$ V, $V_2 = -0.08$ V, $I=-0.20$ mA], which were calculated using the Eq. 12.



Generating training data

To collect the training and validation data required to optimize the NG-RC controller, we perturb the system with a signal that contains 4000 points, and use 2000 points for training and 2000 points for validation. To create the perturbations, we generate uniform random noise with a range of ± 1.5 and zero mean using the `random.uniform` package in NumPy.³⁶ We then filter the noise using a 10th-order low-pass Butterworth filter with a cut-off frequency of 900 Hz, which is implemented using the `signal.butter` package in SciPy.³⁷ The signal is then multiplied by an envelope function so that it can be smoothly repeated on the FPGA if longer training times are required. The signal is then converted to 16-bit values, which are used by the digital-to-analog converter on the FPGA to output a voltage ranging from 0-2.5 V. This voltage is converted to a current using a custom-built voltage-to-current converter, which has the measured transimpedance gain

$$V_{toI}(V_{in}, G) = G \times (-0.3224V_{in} + 0.04082V) / 999.001\Omega, \quad (13)$$

where we use $G = 2.5$. In total, we generate 5 different random signals used to collect 5 different datasets for training and model evaluation. The ridge parameter for each of the 5 datasets is chosen from an array of 100 logarithmically spaced values from 10^{-10} to 10 to minimize the prediction RMSE on the validation set. The same datasets are used to train the one-step ahead and two-step ahead controllers. The learned weights and the ridge regression parameters found for the different datasets and controllers are shown in Supplementary Note 5.

Generating the desired signals

The desired signals are of finite length as they are stored in the FPGA memory. They are repeated every 21 ms. The desired signal for the origin task is a constant $V_{1,des} = 0$. The desired signal for the two USS task is generated using $V_{1,des i} = V_{1ss}' \tanh(\sin(\omega \times i) / b)$, where $\omega = 0.0076$, $b = 0.11$ determines how fast the transition is between the maximum and minimum value, with smaller values being faster, and $V_{1ss}' = 0.571$ is the magnitude of the nonzero fixed-points. This value is 2% smaller than the theoretically predicted value, which was found by

adjusting the desired signal until the control current was approximately zero at the location of the fixed-points. The random waveform control task is generated similarly to the training perturbation, but now the low value is between ± 1.0 , and we use a 20th-order Butterworth low-pass-filter with a cut-off frequency of 2.5 kHz. There is also a smoothing envelope applied to the noise so it can be repeated without any discontinuities. The desired signals are represented using a fixed-point representation, which is described later.

Control performance characterization

The control performance is characterized using RMSE in Eq. 10, but x_i is the desired signal, and \hat{x}_i is the state of the controlled system. The system is controlled once for a specific task using each of the 5 sets of learned weights. The control is turned on after time $t_0 = 7.5$ ms and is turned off after $t_f = 80$ ms. The RMSE of the control is calculated from time $t_1 = 10$ ms to t_f , not including the transient period. The control for each task and set of weights is repeated for values of K ranging from -2 to 1 for the linear controller and ± 1 for the NG-RC-based controllers. In the figures and tables that characterize the RMSE, the error bars and uncertainties are represented by the standard error, which is given by the standard deviation / $\sqrt{\text{num trials}}$, where num trials is 5. The magnitude of the control perturbations is characterized by the root mean square of the signal, or

$$\text{RMS} = \sqrt{\langle u_1^2 \rangle}, \quad (14)$$

which is calculated over the same time interval as the RMSE and uncertainties are reported using the standard error metric.

Power Consumption and Energy Uncertainty

The uncertainty of all stated power consumption and energy is accounted for in the precision of the Rigol DM3068 Digital Multimeter used to measure the current and the voltage of the MPJA DC power supply supplied to the FPGA device.

Fixed-Point Arithmetic

The NG-RC and control law are evaluated using fixed-point arithmetic. All numbers are constrained to 18-bits whenever possible, as the FPGA on-chip only support up to 18×18 bit multiplications. Multiplying numbers with higher precision requires more than one of these multipliers, which would utilize more resources on the FPGA, slow down the computation, and consume more energy.

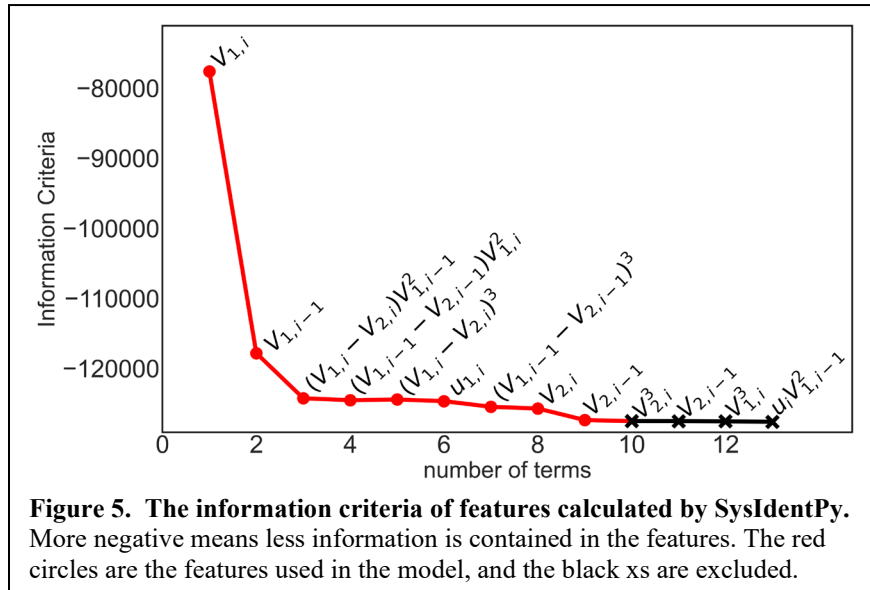
To describe the fixed-point representations, we use the Qm.n format, where Q represents the sign bit, m is the number of integer bits, and n is the number of fractional bits. All the features are represented in the Q0.17 form and the weights are also represented using 18-bits, but their fixed-point representation is adjusted based on the scale of the weights which is affected by the ridge parameter. The representation used for the weights is also used for the feedback gain K , but $\widehat{\mathbf{W}}_u^{-1}$ uses a different representation as the numbers typically require a larger range. The desired signal has the same representation as the features. The different representations of the weights used in the different trials can be seen in Supplementary Note 5.

Quantities that have inherently less precision than 18-bits, such as V_1 and V_2 measured using 12-bit analog to digital converters, and u_1 which is output using a 16-bit digital to analog converter, have the least significant bits padded with 0s to achieve the Q0.17 form.

System Identification

To select the polynomial features used in the NG-RC, we use a regularized version of the routines found in SysIdentPy.²⁸ We provide SysIdentPy with $V_{1,i}$, $V_{2,i}$, $u_{1,i}$ and $V_{1,i} - V_{2,i}$ from an example training dataset, and the model is trained to predict $V_{1,i+1}$. The difference of the voltages is added to the feature dictionary because it appears in the differential equations for the system, but in practice any sum or differences of the system variables may be used.

We use the forward regression orthogonal least squares (FROLS) model, with the nonlinear autoregressive moving average model with exogenous inputs (NARMAX) option. We modify the source code for the estimator to include ridge regression (see Eq. 10) to avoid overfitting and improve model stability.²⁹ We choose the maximum polynomial degree as 3, and we chose the maximum number of time delays to be 2, as these parameters have been found to give good performance.¹⁵ We then use SysIdentPy to calculate the information criteria of all the possible polynomial combinations for those parameters, and limit the number of terms in the information criteria to 30. We choose a relatively large ridge parameter of 10^{-2} as we find it causes the minimum information criteria to occur when less terms are included. The result of this feature selection is shown in Fig. 5.



SysIdentPy finds the minimum information criteria occurs when 14 terms are included in the polynomial, but because the information criteria remains relatively flat after the first 9 terms, hence we select only these to reduce the model complexity. We also include $u_{1,i-1}$ as we found it improves the control. We do not use the weights learned by SysIdentpy, instead we manually code these polynomial features into our custom Python code that trains and validates the model, which is then transferred to the FPGA.

Software and devices

The FPGA is compiled and resources are estimated using Quartus Prime 21.1, the training, validation, and analysis of the controlled system is done in Python 3.9.0, using Numpy 1.24.3, Scipy 1.11.1, and the fixed-point calculations are replicated using fxpmath³⁸ 0.4.8 on an x86-64 CPU running Windows 11. The FPGA is the Max 10 10M50DAF484C6G on a Terasic Max 10 Plus development board.

Data Availability

The data used to create each figure in this manuscript and the Supplementary Material are available in figshare with the identifier “doi: 10.6084/m9.figshare.25534552”.³⁹

Code Availability

The Python and FPGA code with example data are available in figshare with the identifier “doi: 10.6084/m9.figshare.25534621”.⁴⁰

Acknowledgements

We gratefully acknowledge the financial support of the U.S. Air Force Office of Scientific Research, Contract #FA9550-22-1-0203.

Author Contributions

R. K. and W. A. S. B. performed the experimental studies and analysis. D. J. G. developed the basic control algorithm, interpreted the results, and supervised the work. All authors prepared the manuscript.

Competing Interests

Daniel Gauthier is a co-founder of ResCon Technologies, LLC, which is commercializing the application of reservoir computing. The remaining authors declare no competing interests.

References

1. Chowdhary, K. R. Natural Language Processing. in *Fundamentals of Artificial Intelligence* 603–649 (Springer, New Delhi, 2020).
2. Martins, J. R. R. A. & Ning, A. *Engineering Design Optimization*. (Cambridge University Press, Cambridge, 2021).
3. Qayyum, A., Usama, M., Qadir, J. & Al-Fuqaha, A. Securing Connected & Autonomous Vehicles: Challenges Posed by Adversarial Machine Learning and the Way Forward. *IEEE Commun. Surv. Tutor.* **22**, 998–1026 (2020).
4. Ott, E., Grebogi, C. & Yorke, J. A. Controlling chaos. *Phys. Rev. Lett.* **64**, 1196–1199 (1990).
5. Pyragas, K. Continuous control of chaos by self-controlling feedback. *Phys. Lett. A* **170**, 421–428 (1992).
6. Ahmed, I., Quiñones-Grueiro, M. & Biswas, G. Fault-Tolerant Control of Degrading Systems with On-Policy Reinforcement Learning. *IFAC-Pap.* **53**, 13733–13738 (2020).

7. Nguyen, N., Krishnakumar, K., Kaneshige, J. & Nespeca, P. Flight Dynamics and Hybrid Adaptive Control of Damaged Aircraft. *J. Guid. Control Dyn.* **31**, 751–764 (2008).
8. Khan, S. & Yairi, T. A review on the application of deep learning in system health management. *Mech. Syst. Signal Process.* **107**, 241–265 (2018).
9. Mehonic, A. & Kenyon, A. J. Brain-inspired computing needs a master plan. *Nature* **604**, 255–260 (2022).
10. Modha, D. S. *et al.* Neural inference at the frontier of energy, space, and time. *Science* **382**, 329–335 (2023).
11. Zhang, W. *et al.* Edge learning using a fully integrated neuro-inspired memristor chip. *Science* **381**, 1205–1211 (2023).
12. Jaeger, H. & Haas, H. Harnessing Nonlinearity: Predicting Chaotic Systems and Saving Energy in Wireless Communication. *Science* **304**, 78–80 (2004).
13. Maass, W., Natschläger, T. & Markram, H. Real-Time Computing Without Stable States: A New Framework for Neural Computation Based on Perturbations. *Neural Comput.* **14**, 2531–2560 (2002).
14. Canaday, D., Pomerance, A. & Gauthier, D. J. Model-free control of dynamical systems with deep reservoir computing. *J. Phys. Complex.* **2**, 035025 (2021).
15. Gauthier, D. J., Bollt, E., Griffith, A. & Barbosa, W. A. S. Next generation reservoir computing. *Nat. Commun.* **12**, 5564 (2021).
16. Chang, A., Bienfang, J. C., Hall, G. M., Gardner, J. R. & Gauthier, D. J. Stabilizing unstable steady states using extended time-delay autosynchronization. *Chaos Interdiscip. J. Nonlinear Sci.* **8**, 782–790 (1998).
17. Romeiras, F. J., Grebogi, C., Ott, E. & Dayawansa, W. P. Controlling chaotic dynamical systems. *Phys. Nonlinear Phenom.* **58**, 165–192 (1992).
18. Gauthier, D. J. Resource Letter: CC-1: Controlling chaos. *Am. J. Phys.* **71**, 750–759 (2003).
19. Ariyur, K. B. & Krstic, M. *Real Time Optimization by Extremum Seeking Control*. (John Wiley & Sons, Inc., USA, 2003).
20. Blakely, J. N., Illing, L. & Gauthier, D. J. Controlling Fast Chaos in Delay Dynamical Systems. *Phys. Rev. Lett.* **92**, 193901 (2004).
21. Sarangapani, J. *Neural Network Control of Nonlinear Discrete-Time Systems*. (CRC Press, Boca Raton, Fla., 2006).
22. Slotine, J.-J. E. & Li, W. *Applied Nonlinear Control*. (Prentice-Hall, Englewood Cliffs, NJ, 1991).

23. Kent, R. M., Barbosa, W. A. S. & Gauthier, D. J. Controlling chaotic maps using next-generation reservoir computing. *Chaos Interdiscip. J. Nonlinear Sci.* **34**, 023102 (2024).
24. Gonon, L. & Ortega, J.-P. Reservoir Computing Universality With Stochastic Inputs. *IEEE Trans. Neural Netw. Learn. Syst.* **31**, 100–112 (2020).
25. Waegeman, T., Wyffels, F. & Schrauwen, F. Feedback control by online learning an inverse model. *IEEE Trans. Neural Netw. Learn. Syst.* **23**, 1637–1648 (2012).
26. Zhai, Z.-M. *et al.* Model-free tracking control of complex dynamical trajectories with machine learning. *Nat. Commun.* **14**, 5698 (2023).
27. Boltt, E. On explaining the surprising success of reservoir computing forecaster of chaos? The universal machine learning dynamical system with contrast to VAR and DMD. *Chaos Interdiscip. J. Nonlinear Sci.* **31**, 013108 (2021).
28. Lacerda, W. R., Andrade, L. P. C. da, Oliveira, S. C. P. & Martins, S. A. M. SysIdentPy: A Python package for System Identification using NARMAX models. *J. Open Source Softw.* **5**, 2384 (2020).
29. Chen, S., Chng, E. S. & Alkadhimi, K. Regularized orthogonal least squares algorithm for constructing radial basis function networks. *Int. J. Control* **64**, 829–837 (1996).
30. Socolar, J. E. S., Sukow, D. W. & Gauthier, D. J. Stabilizing unstable periodic orbits in fast dynamical systems. *Phys. Rev. E* **50**, 3245–3248 (1994).
31. Shinbrot, T., Ott, E., Grebogi, C. & Yorke, J. A. Using chaos to direct trajectories to targets. *Phys. Rev. Lett.* **65**, 3215–3218 (1990).
32. Kostelich, E. J., Grebogi, C., Ott, E. & Yorke, J. A. Higher-dimensional targeting. *Phys. Rev. E* **47**, 305–310 (1993).
33. Sukow, D. W., Bleich, M. E., Gauthier, D. J. & Socolar, J. E. S. Controlling chaos in fast dynamical systems: Experimental results and theoretical analysis. *Chaos* **7**, 560–576 (1997).
34. Barbosa, W. A. S. & Gauthier, D. J. Learning spatiotemporal chaos using next-generation reservoir computing. *Chaos Interdiscip. J. Nonlinear Sci.* **32**, 093137 (2022).
35. Vogel, C. R. *Computational Methods for Inverse Problems*. (Society for Industrial and Applied Mathematics, 2002).
36. Harris, C. R. *et al.* Array programming with NumPy. *Nature* **585**, 357–362 (2020).

37. Virtanen, P. *et al.* SciPy 1.0: Fundamental Algorithms for Scientific Computing in Python. *Nat. Methods* **17**, 261–272 (2020).
38. Alcaraz, F. fxpmath. <https://github.com/francof2a/fxpmath> (2020).
39. Kent, R. M., Barbosa, W. A. S. & Gauthier, D. J. Controlling Chaos Using Edge Computing Hardware Data sets. *figshare* <https://doi.org/10.6084/m9.figshare.25534552> (2024).
40. Kent, R. M., Barbosa, W. A. S. & Gauthier, D. J. Controlling Chaos Using Edge Computing Hardware code. *figshare* <https://doi.org/10.6084/m9.figshare.25534621> (2024).
41. Dedania, R. & Jun, S.-W. Very Low Power High-Frequency Floating Point FPGA PID Controller. in *Proceedings of the 12th International Symposium on Highly-Efficient Accelerators and Reconfigurable Technologies* 102–107 (2022)
42. Li, Y., Li, S. E., Jia, X., Zeng, S. & Wang, Y. FPGA accelerated model predictive control for autonomous driving. *Journal of Intelligent and Connected Vehicles* **5**, 63–71 (2022).
43. Hartley, E. N. *et al.* Predictive Control Using an FPGA With Application to Aircraft Control. *IEEE Transactions on Control Systems Technology* **22**, 1006–1017 (2014).
44. Modular ADC Core Intel® FPGA IP and Modular Dual ADC Core Intel®... *Intel* <https://www.intel.com/content/www/us/en/docs/programmable/683596/20-1/and-references.html>.

Supplementary Information

Controlling Chaos Using Edge Computing Hardware

Robert M. Kent, Wendson A.S. Barbosa, and Daniel J. Gauthier

May 8, 2024

Supplementary Note 1: Comparing complexity with previous reservoir computing approach

In this section, we compare the complexity of the controller based on traditional reservoir computing by Canaday *et al.*¹⁴ to our approach based on next-generation reservoir computing. We highlight three key metrics: the number of multiplications required to evaluate the control law which dominates the energy and space requirements on the FPGA, the number of tanh evaluations which requires look up tables, and the size of the total feature vector which affects the number of trainable parameters. Throughout this section, we use our notation to describe the traditional reservoir computing approach.

Inverse control with traditional reservoir computing

In the work by Canaday *et al.*,¹⁴ evaluating the control law requires computing the updated reservoir state, which is analogous to computing the total feature vector $\mathbb{O}_{total,i} \in \mathbb{R}^N$ in our approach, then the reservoir state is mapped onto the control perturbation u_i used to drive the system to the desired state. We examine the mapping form of the reservoir state obtained from the differential form using an Euler integration method, as this is the form computed by the FPGA. The state of a reservoir with N nodes is given by

$$\mathbb{O}_{total,i} = \alpha \tanh(\mathbf{A}\mathbb{O}_{total,i-1} + \mathbf{W}_{in}^x \mathbf{X}_i + \mathbf{W}_{in}^{des} \mathbf{Y}_{des,i+m} + \mathbf{b}) + (1 - \alpha) \mathbb{O}_{total,i-1}, \quad (1)$$

where $\alpha = \Delta t/c$, Δt is the timestep of the integration, c is the time constant, $\mathbf{A} \in \mathbb{R}^{N \times N}$ is the adjacency matrix determining the connections between nodes in the reservoir, $\mathbf{W}_{in}^x \in \mathbb{R}^{N \times d'}$ maps the accessible system variables \mathbf{X}_i into the reservoir, $\mathbf{W}_{in}^{des} \in \mathbb{R}^{N \times d'}$ maps the desired state $\mathbf{Y}_{des,i+m} \in \mathbb{R}^{d'}$ into the reservoir, and $\mathbf{b} \in \mathbb{R}^N$ is a bias vector. The mapping of the reservoir state onto the control perturbations is given by

$$\mathbf{u}_i = \mathbf{W}\mathbb{O}_{total,i}, \quad (2)$$

where $\mathbf{W} \in \mathbb{R}^{d \times N}$ are the weights learned through ridge regression.

The number of multiplications required by the model is dominated by the sparsity of \mathbf{A} , which is characterized by the number of nonzero elements k in each row. The total number of multiplications contributed by each term are kN from $\mathbf{A}\mathbb{O}_{total,i-1}$, $2Nd'$ from $\mathbf{W}_{in}^x \mathbf{X}_i$ and $\mathbf{W}_{in}^{des} \mathbf{Y}_{des,i+m}$, $2N$ from $\alpha \tanh(\dots)$ and $\alpha \mathbb{O}_{total,i-1}$, and dN from $\mathbf{W}\mathbb{O}_{total,i}$. If $\mathbb{O}_{total,i-1}$ is subtracted from $\tanh(\dots)$ before they are multiplied by α , the total number of multiplications are reduced by N , and we assume this best-case scenario. To control the chaotic circuit, Canaday *et al.*¹⁴ uses $k = 3$, $N = 30$, $d' = 2$, and $d = 1$, which requires 270 multiplications, 30 trainable

parameters, and 30 evaluations of \tanh . Recall that Canaday *et al.*¹⁴ requires a two layer controller to achieve accurate control, which doubles the resources to 540 multiplications, 60 evaluations of \tanh , and 60 trainable parameters. This arithmetic is implemented using 32-bit fixed-point arithmetic, but the FPGA has only 18×18 -bit multipliers, meaning that additional multipliers are needed for a single multiplication.

Control with next-generation reservoir computing

In our approach, evaluating the control law involves computing the feature vector $\mathbb{O}_{F,i} \in \mathbb{R}^{N-d}$, and then \mathbf{u}_i is computed directly using the control law

$$\mathbf{u}_i = \widehat{\mathbf{W}}_u^{-1} [\mathbf{Y}_{des,i+m} - \widehat{\mathbf{W}}_F \mathbb{O}_{F,i} + \mathbf{K} \mathbf{e}_i]. \quad (3)$$

The number of multiplications is dominated by the polynomial functions in $\mathbb{O}_{F,i}$, whose number and complexity are determined using system identification techniques,^{2,3} and depend on the dynamics of the system under control. For now, we count only the contributions from matrix multiplications in Eq. 3, which are $d(N-d)$ from $\widehat{\mathbf{W}}_F \mathbb{O}_{F,i}$, d^2 from $\mathbf{K} \mathbf{e}_i$, and d^2 from $\widehat{\mathbf{W}}_u^{-1}[\dots]$.

To control the chaotic circuit, we use $N = 10$, $d = 1$, and $\mathbb{O}_{F,i}$ is given by

$$\mathbb{O}_{F,i} = [u_{1,i-1}, V_{1,i}, V_{1,i-1}, (V_{1,i} - V_{2,i})V_{1,i-1}^2, (V_{1,i-1} - V_{2,i-1})V_{1,i}^2, (V_{1,i} - V_{2,i})^3, (V_{1,i-1} - V_{2,i-1})^3, V_{2,i}, V_{2,i-1}], \quad (4)$$

which requires three multiplications for each cubic term, bringing the total number of multiplications to 23. However, we employ a trick to reduce the number of multiplications further by noting that some multiplications are time delayed versions of each other, allowing us to reuse them in future evaluations of the control law. Specifically, $(V_{1,i} - V_{2,i})^3$ becomes $(V_{1,i-1} - V_{2,i-1})^3$, saving three multiplications, and $V_{1,i}^2$ becomes $V_{1,i-1}^2$, saving two multiplications. This brings the total number of multiplications per evaluation of the control law to 18, the number of trainable parameters to 10, and no evaluation of \tanh is required. The arithmetic is implemented using 18-bit fixed-point arithmetic, which is well matched to the multipliers on the FPGA and therefore uses even fewer multipliers than the Canaday approach.

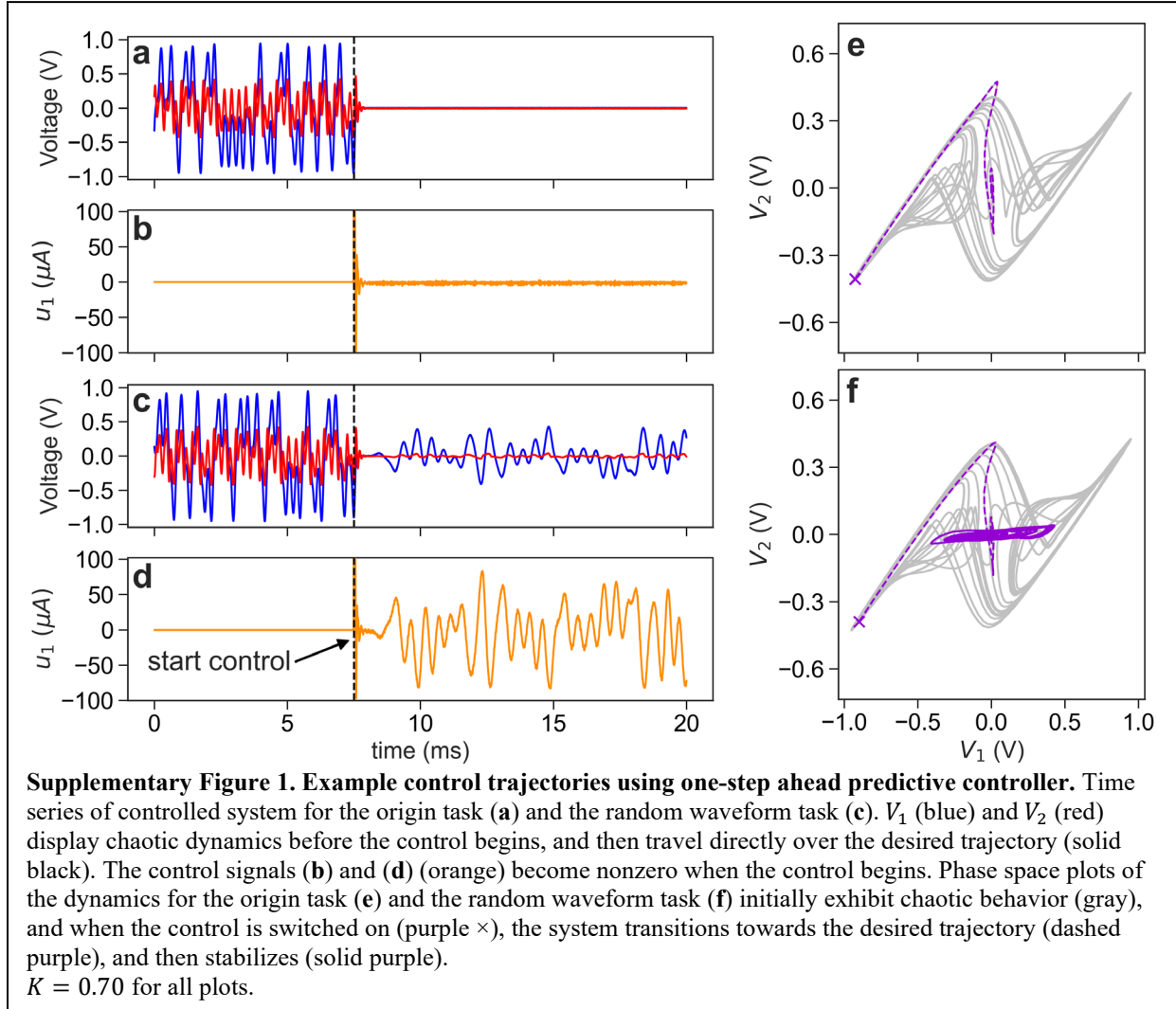
Comparing our approach directly to the one-layer controller, we require $15 \times$ fewer multiplications, a $3 \times$ fewer trainable parameters, and 30 fewer evaluations of \tanh . For the two-layer controller, which is more comparable to our approach in terms of performance, we require $30 \times$ fewer multiplications, $6 \times$ fewer trainable parameters, and 60 fewer evaluations of \tanh .

Supplementary Note 2: Time-series trajectories for the origin and random waveform tasks

Supplementary Fig. 1 shows example trajectories during control for the origin task and the random waveform task for a given K . For the origin task, the system is initially far from the desired point but is quickly steered there and remains stable for the rest of the control period with no visible ringing. It is notable that the control signal required to stabilize the system here is very small, unlike in Canaday *et al.*¹⁴ For the random waveform task, the system follows the desired

trajectory without any visible deviation from the desired signal, despite the great difficulty of this problem.

Supplementary Note 3: Additional performance metrics



In this section, we compare additional performance metrics for the linear, and NG-RC-based controllers with one and two-step ahead prediction. These performance metrics include the control error and size of the control perturbations as a function of the feedback control gain K , and the sensitivity to control loop latency.

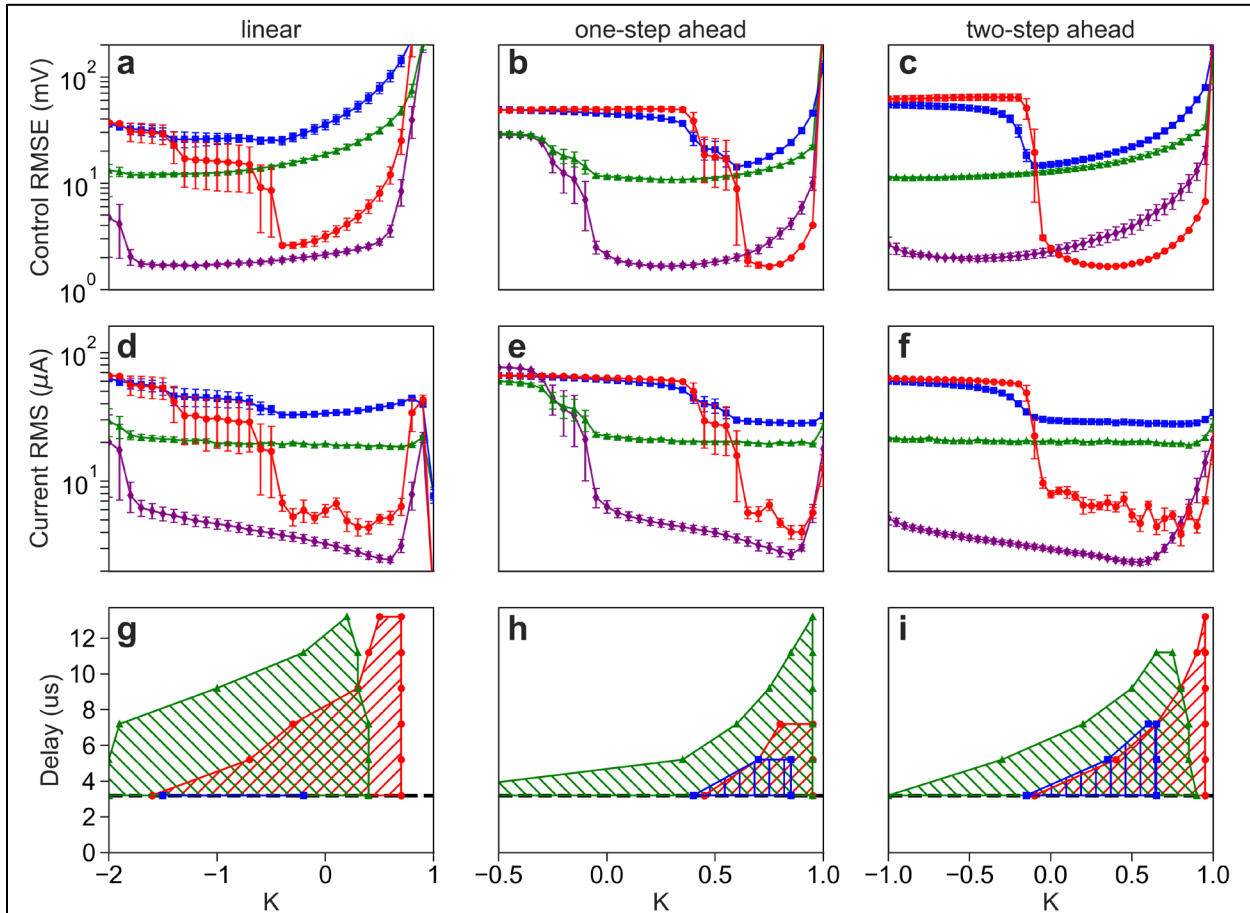
The error for each controller type and task as K varies is shown in Supplementary Fig. 2a-c. We see that the domain of control is the largest for both the origin task and the two USS task for the linear and two-step ahead controller. However, the two-step ahead controller has a significantly larger domain of control compared to the linear controller for the random waveform task.

The one-step ahead controller generally has a smaller range of stable K values than the other two controllers, but comparable minimum errors to the two-step ahead controller. We believe that the two-step ahead controller has better performance for multiple reasons. The first is that

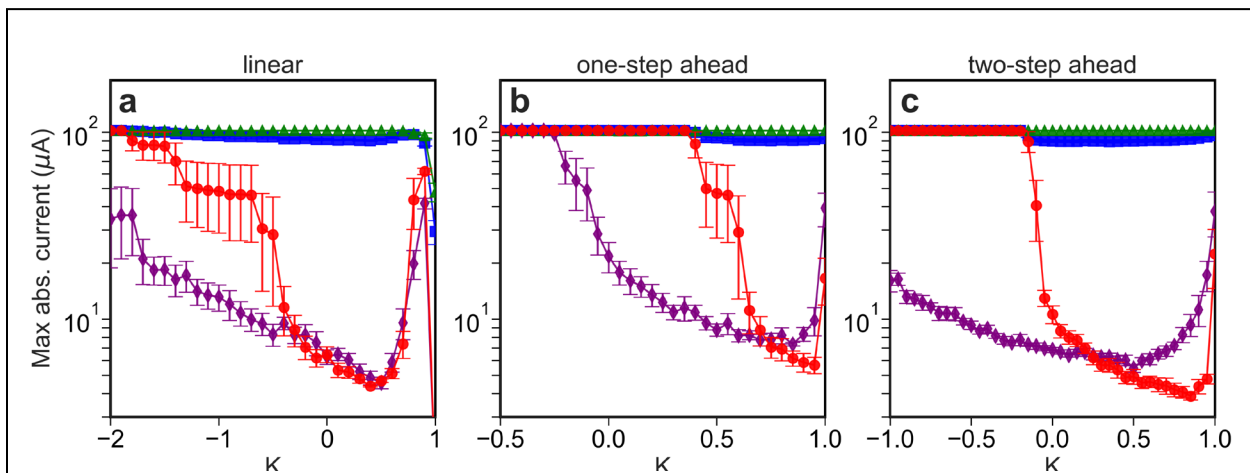
the latency between measuring the state and applying the control perturbations is a significant fraction of the sample time, so the state of the system one-step ahead is not sufficiently affected by the control perturbation at the current step, and the ML model cannot accurately approximate \mathbf{W}_u . The second is that the sensitive dependence to initial conditions present in chaos guarantees that states further in the future are increasingly sensitive to the control perturbation at the current time, so the ML must more accurately approximate \mathbf{W}_u to achieve good prediction performance. Despite the differences between the one-step and two-step ahead controllers, both have significantly lower minimum errors than the linear controller, especially for the random waveform task, showing the robustness of our approach.

The RMS of the control perturbations are shown in Supplementary Fig. 2d-f, and the RMS values that correspond to the minimum control RMSE are shown in Supplementary Table 1. We also show the maximum absolute value of the RMS current after the transient period of 2.5 ms in Supplementary Fig. 3. We see that the size of the control perturbations when the system is stabilized at the origin are larger than when the system is stabilized at either USS at the center of the scrolls for all controllers. However, the linear controller requires larger control perturbations for the random waveform task than the other controllers, demonstrating the effectiveness of our approach.

It is important to characterize how the stability of the system is affected by the control loop latency and the feedback gain K , called the domain of control, which is useful for situations where this latency may drift between the training and control phase. The domain of control for each controller and control task are shown in Supplementary Fig. 2g-i, where the control is classified as stable when the error is below 30 mV. We see that the linear controller has the largest domains of control for the origin task and two USS tasks but fails to maintain stability on the random waveform task as the latency is increased, in contrast to the two-step ahead controller that maintains stability for this task with up to 4 μ s of added delay.



Supplementary Figure 2. Performance of the NG-RC controller. a-c RMSE of control, d-f RMS of control current, and g-i domain of control for the linear, one and two-step ahead NG-RC controllers for the origin task (red circles), two USS task (green triangles), random waveform task (blue squares), and the two USS task excluding transitions (purple diamonds).



Supplementary Figure 3. Maximum control current. a-c Maximum absolute value of the control current after the transient period of 2.5ms for the linear, one and two-step ahead NG-RC controllers for the origin task (red circles), two USS task (green triangles), random waveform task (blue squares), and the two USS task excluding transitions (purple diamonds).

Supplementary Table 1 RMS of control current

Controller type	Origin task	Two USS task	Two USS task (No transients)	Random Waveform Task
Linear	$6.79 \pm 0.97 \text{ uA}$	$21.88 \pm 1.21 \text{ uA}$	$4.94 \pm 0.49 \text{ uA}$	$37.17 \pm 4.16 \text{ uA}$
one-step ahead	$6.54 \pm 0.63 \text{ uA}$	$20.49 \pm 0.47 \text{ uA}$	$4.54 \pm 0.31 \text{ uA}$	$29.75 \pm 0.72 \text{ uA}$
two-step ahead	$6.84 \pm 0.92 \text{ uA}$	$21.09 \pm 0.27 \text{ uA}$	$3.55 \pm 0.16 \text{ uA}$	$31.24 \pm 0.78 \text{ uA}$

The stated values are the RMS of the control current when the control error (RMSE) is minimized with uncertainty derived from the standard error over five trials.

Supplementary Note 4: Comparing control resources

We compare the speed of our controller, the power consumption, and the resource utilization of the FPGA with other nonlinear control studies in Supplementary Table 2. The computational complexity of each of these control tasks is different, so the comparison should only be used as an approximate guide. The energy per inference is calculated using the sampling rate.

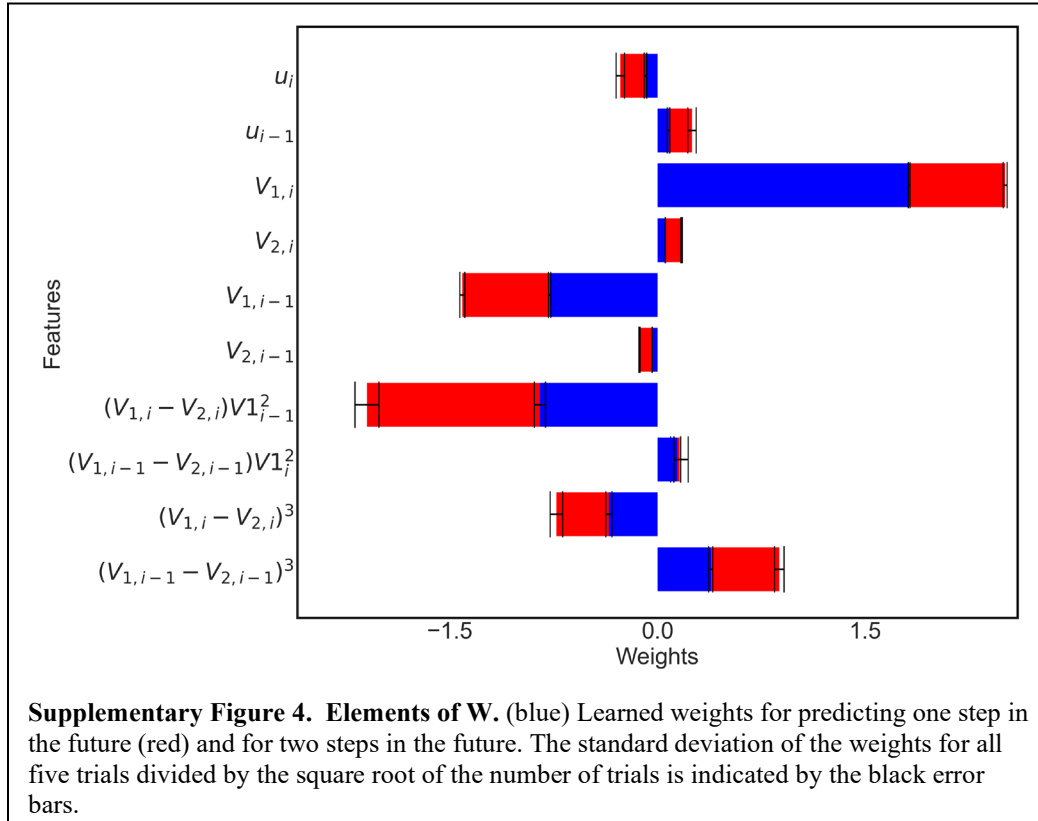
Supplementary Table 2 Comparing control resources with other FPGA control work

	This Work	Dedania 2022 ⁴¹	Li 2022 ⁴²	Hartley 2014 ⁴³
Task	Chaotic circuit control	Low power PID control	Autonomous Driving	Aircraft control
Model	NG-RC Controller (one-step ahead)	PID Control	Model Predictive Control	Model Predictive Control
Total Power	$1384.0 \pm 0.7 \text{ mW}$	20 mW	6 W	9.75 W
Dynamic Power	–	–	2.5 W (chip power)	5.469 W
ML Power	$5.0 \pm 1.4 \text{ mW}$	–	–	–
Solution time	50 ns	–	0.0803 ms (average)	4 ms (max)
Sampling rate	$5 \mu\text{s}$	$1.58 \mu\text{s}$	20 ms	0.2 s
Energy per Inference (J)	$25.0 \pm 7.0 \text{ nJ}$ (ML only) ($6920.0 \pm 3.5 \text{ nJ}$ total)	31.54 nJ	50 mJ (chip power) 120 mJ (total)	1.094 J (dynamic) (1.95 J total)
Registers	924 (2 %)	3998 (Logic Cells)(75%)	30059 (Flip flops) (28%)	145526 (49%)
LUT	1497 (3%)	-	47923 (90%)	111132 (7%)
Multipliers	18 (18b \times 18b) (13%)	3 (18b \times 18b) (37%)	78 (18b \times 25b) (35%)	602 (18b \times 25b) (78%)
Block Memory	1 (<1%) (9Kb) (9216 total bits)	26 (86%) (4Kb) (104000 total bits)	22 (7%) (18Kb) (~396000 total bits)	142 (34%) (36Kb) (5112000 total bits)

The control resources used for different control algorithms implemented on an FPGA for different control tasks. The “–” denotes that this information is unavailable.

Supplementary Note 5: Elements of W and prediction performance on validation data

For each of the five trials, the weights are learned using different training and validation sets, generated from a different random perturbation. Some of these weights are trained for one-step-ahead prediction ($V_{1,i+1}$) or for two-step-ahead prediction ($V_{1,i+2}$) in the future. The weights are visualized in Supplementary Fig. 4.



For one-step- (two-step-) ahead prediction, the ridge regression parameter giving the minimum prediction error on the validation set, the minimum prediction error, and the fixed-point format are given in Supplementary Table 3 (Supplementary Table 4).

Supplementary Table 3 Prediction performance and Parameters for One-Step-Ahead Prediction

Trial Number	Min. Prediction RMSE (mV)	Ridge Parameter	Fixed point representation for \mathbf{W}	Fixed point representation for W_u^{-1}
1	2.28	1.29×10^{-7}	Q2.15	Q4.13
2	2.09	2.78×10^{-8}	Q2.15	Q5.12
3	2.15	7.74×10^{-5}	Q2.15	Q4.13
4	2.16	3.59×10^{-5}	Q2.15	Q4.13
5	2.16	2.78×10^{-5}	Q2.15	Q4.13

The minimum prediction RMSE, the optimal ridge parameter, and the fixed-point representation for \mathbf{W} and W_u^{-1} are given for each trial for the one-step ahead prediction model.

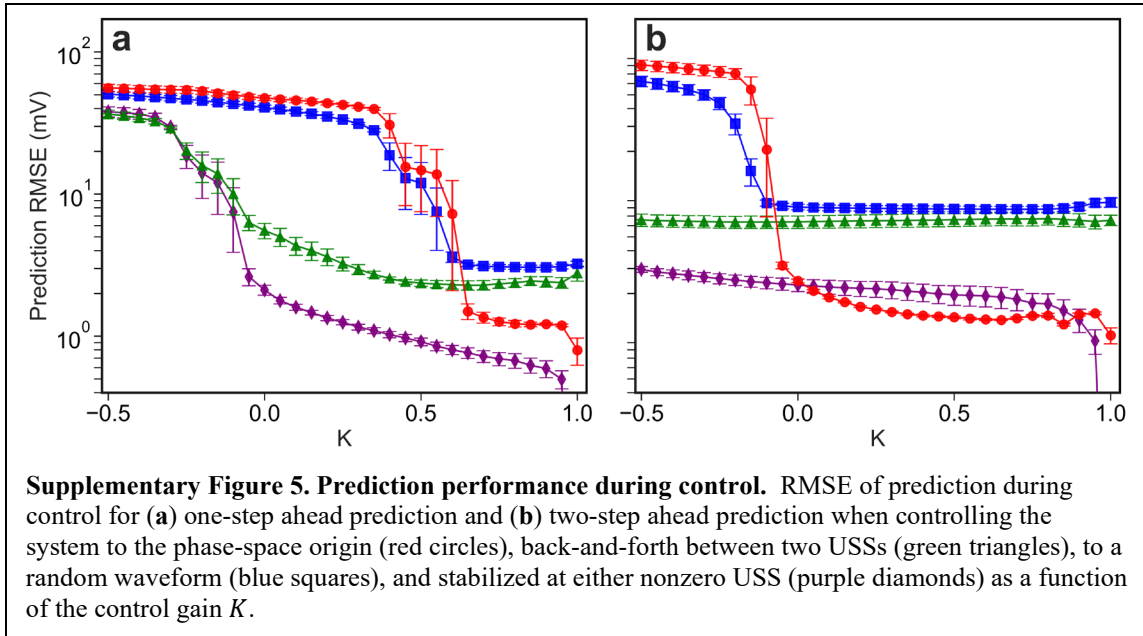
Supplementary Table 4 Prediction Performance and Parameters for Two-Step-Ahead Prediction

Trial Number	Min. Prediction RMSE (mV)	Ridge Parameter	Fixed point representation for \mathbf{W}	Fixed point representation for W_u^{-1}
1	4.58	2.78×10^{-8}	Q2.15	Q2.15
2	3.88	1.00×10^{-5}	Q2.15	Q3.14
3	4.39	7.74×10^{-5}	Q2.15	Q3.14
4	4.23	1.66×10^{-5}	Q2.15	Q2.15
5	3.99	1.29×10^{-5}	Q2.15	Q2.15

The minimum prediction RMSE, the optimal ridge parameter, and the fixed-point representation for \mathbf{W} and W_u^{-1} are given for each trial for the two-step ahead prediction model.

Supplementary Note 6: Prediction performance during control

In this section, we quantify the prediction performance while the controller is active as a function of some of the control parameters such as the feedback gain K , which can be seen for both the one-step- and two-step-ahead prediction in Supplementary Fig. 5. Like the control error presented in Fig. 3 of the main text, the prediction error for all tasks is small for only a fixed range of K values. Notably, this range is larger for predicting two steps in the future, but the minimum RMSE for each task is higher. The minimum prediction RMSE for each task are listed in Supplementary Table 5. This minimum prediction error vs. stability trade-off is an important consideration when designing an NG-RC controller.



Supplementary Table 5 Prediction performance during control

Controller type	Origin task	Two USS task	Two USS task (no transients)	Random Waveform task
one-step ahead	1.19 ± 0.02 mV	2.28 ± 0.17 mV	0.50 ± 0.07 mV	3.04 ± 0.11 mV
two-step ahead	1.21 ± 0.03 mV	6.36 ± 0.63 mV	0.93 ± 0.18 mV	7.82 ± 0.37 mV

The minimum prediction RMSE during the control loop for the one and two-step ahead controllers for each control task, where the error for $K = 1$ has been excluded because the origin and two USS task (no transients) have significantly lower prediction errors here but control fails.

Supplementary Note 7: Controller latency

In this section, we characterize the minimum latency of the controller because it can affect the domain of control. We find that the latency, defined as the minimum time it takes for an adjustment to exit the controller in response to a change in the input in the absence of the ML model, is a function of the sample rate. We believe the latency is due to the anti-aliasing low-pass filter before the analog-to-digital converter and the serial protocol for transferring data from the analog-to-digital and digital-to-analog converters used to communicate between the FPGA and these off-chip devices. We use the maximum clock rates suggested by the Modular Dual ADC core IP⁴⁴ in Quartus Prime 21.1, which range from 1 MHz to 80 MHz depending on the chosen sampling rate, and use a constant 30 MHz clock for the digital-to-analog converter, the maximum allowed by these devices.

We characterized the latency by feeding the analog-to-digital converter with a saw-tooth waveform using the Stanford Research Systems DS345, pass the corresponding digital values directly to the digital-to-analog converter, and measure the output using a Tektronix TDS 210 oscilloscope. The results of this measurement is shown in Supplementary Fig. 6. The minimum latency is $2.5 \mu\text{s}$ for the sample rate 1 Msamples/s. For this reason, we use this sample rate in

our experiment even though the controller operates at a rate of 200 kHz. We also find that our custom-build voltage-to-current converter adds an additional delay of $0.7 \mu\text{s}$ independent of sample rate. Additionally, the digital-to-analog converter on the FPGA device has peak to peak settling times of over $2 \mu\text{s}$, limiting the rate at which the control perturbations can be switched.

